remote sensing

MDPI

Article

Predicting Sea-Level Extremes and Wetland Change in the Maroochy River Floodplain Using Remote Sensing and Deep Learning Approach

Nawin Raj [1,*], Niharika Singh [2], Nathan Downs [1] and Lila Singh-Peterson [3]

[1] School of Mathematics, Physics and Computing, Springfield Campus, University of Southern Queensland, Springfield, QLD 4300, Australia; nathan.downs@unisq.edu.au
[2] UniSQ College (Pathways), Springfield Campus, University of Southern Queensland, Springfield, QLD 4300, Australia; niharika.singh@unisq.edu.au
[3] School of Agriculture and Environmental Science, Springfield Campus, University of Southern Queensland, Springfield, QLD 4300, Australia; lila.singh-peterson@unisq.edu.au
* Correspondence: nawin.raj@unisq.edu.au

Abstract

Wetlands are an important part of coastal ecosystems but are under increasing pressure from climate change-induced sea-level rise and flooding, in addition to development pressures associated with increasing human populations. The change in tidal events and their intensity due to sea-level rise is also reshaping and challenging the vitality of existing wetland systems, requiring more intensive localized studies to identify future-focused restoration and conservation strategies. To support this endeavor, this study utilizes tide gauge datasets from the Australian Bureau of Meteorology (BOM) for maximum sea-level (Hmax) prediction and Landsat Collection surface reflectance datasets obtained from the United States Geological Survey (USGS) database to detect and project patterns of change in the Maroochy River floodplain of Queensland, Australia. This study developed an efficient hybrid deep learning model combining a Convolutional Neural Network and Bidirectional Long Short-Term Memory (CNNBiLSTM) architecture for the prediction of maximum sea-level and tidal events. The proposed model significantly outperformed three benchmark models (Multiple Linear Regression (MLR), Support Vector Regression (SVR), and CatBoost) in achieving a high correlation coefficient (r = 0.9748) for maximum sea-level prediction. To further address the increasing frequency and intensity of tidal events linked to sea-level rise, a CNNBiLSTM classification model was also developed, achieving 96.72% accuracy in predicting extreme tidal occurrences. This study identified a significant positive linear increase in sea-level rise of 0.016 m/year between 2014 and 2024. Wetland change detection using Landsat imagery along the Maroochy River floodplain also identified a substantial vegetation loss of 395.64 hectares from 2009 to 2023. These findings highlight the strong potential of integrating deep learning and remote sensing for improved prediction and assessment of sea-level extremes and coastal ecosystem changes. The study outcomes provide valuable insights for informing not only conservation and restoration activities but also for providing localized projections of future change necessary for the progression of effective climate adaptation and mitigation strategies.

Keywords: CNNBiLSTM bidirectional long short-term memory (BiLSTM); convolutional neural network (CNN); deep learning (DL); machine learning (ML); maximum sea level (Hmax); support vector regression (SVR); categorical boosting (CatBoost); multilinear regression (MLR); successive variational mode decomposition (SVMD)

Academic Editors: Xiyong Hou, Chao Chen, Peng Li and Qi Wang

Received: 8 July 2025
Revised: 19 August 2025
Accepted: 22 August 2025
Published: 28 August 2025

Citation: Raj, N.; Singh, N.; Downs, N.; Singh-Peterson, L. Predicting Sea-Level Extremes and Wetland Change in the Maroochy River Floodplain Using Remote Sensing and Deep Learning Approach. *Remote Sens.* **2025**, *17*, 2988. https://doi.org/10.3390/rs17172988

1. Introduction

Wetlands are an important part of coastal ecosystems but are under increasing pressure from climate change-induced sea-level rise and flooding, as well as from development pressures associated with increasing human populations [1]. The health and vitality of wetlands are considered to be a critical factor in positively contributing to a number of United Nations Sustainable Development Goals [2]. The response of wetland areas to these extreme impacts occurs on a varying timescale, spanning near-instantaneous vegetation loss after nearby land reclamation [3] to long-term lagged effects exacerbated by climate change [4]. Blue carbon sequestered and stored by coastal wetlands plays an important role in regulating the global carbon balance [4]. Climate change factors and soil degradation due to anthropogenic activities, however, continuously degrade the vitality of wetland ecosystems, which, in turn, compromises the systems' capacity to regulate the carbon balance [3]. This cyclic relationship will continue unabated whilst 0.15–1.02 Pg of CO_2 emissions continues to be released into the atmosphere [5]. Although there are many abiotic and biotic factors that influence the health and functionality of wetlands, climate change is identified as a major threat.

Coastal wetlands in Australia range from extensive mangrove forests and sabkha plains in the tropical north to numerous fronted estuaries, drowned river valleys, and coastal embayment [6]. Tasmania is the only island state where mangroves are absent. According to [6], observations in past decades indicate that recent anthropogenic climate change has significantly impacted the Australian coastline. The key aspects of these climate-induced impacts relate to accelerating sea-level rise with saline intrusion, mangrove encroachment and *Melaleuca* dieback [6]. Due to the position of coastal wetlands, which are located in the intertidal zone, these ecosystems are highly vulnerable to sea-level rise and tidal inundation [7]. The rise in the sea level with increased inundation and salinity also affects the shape and span of the wetlands and habitats of wetland species [8]. For example, previous research [9] examining the southeast Australian coast analyzed wetland lateral accommodation in 110 estuaries under a high sea-level rise scenario. The study showed that, under this scenario, saline wetlands were at risk of disappearing from open–closed estuaries if they could not vertically accrete at the pace equal to, or greater than, the rate of sea-level rise. Wetland environments are challenging to work in, as some areas are difficult and time-consuming to access and quantify [10]. Despite these challenges, and due to their important functions, monitoring wetlands is important, as Guo et al. [11] found that wetlands have dramatically declined in the last 50 years due to pollution in some regions of the world.

Other studies from around the world have also identified that the rise in maximum sea level (Hmax) during tidal events poses an increasing threat to wetland ecosystems [12,13]. According to [14], a large portion of Mediterranean coastal marshes will be lost due to sea-level rise by 2100. As a result of increasing mean sea levels, a study on coastal inundation in Sydney, Australia, reported that as sea levels rise, severe floods will become more frequent with high tidal events [15]. Another study located in northern New South Wales, Australia, identified that the combination of spring tides, ocean surface climate drivers, the Southern Oscillation Index (SOI), and the Pacific Decadal Oscillation (PDO) is a significantly positive indicator of high sea levels and extreme coastal erosion [16]. These studies further highlight that sea-level rise and associated coastal inundation are largely driven by a combination of lunar effects on tides and the trapping of solar radiation in the Earth's atmosphere producing enhanced climate change impacts. Accordingly, the thresholds used to identify climate risk in these environments cannot remain fixed but, rather, should be relative to these changing background conditions and specific locational nuances.

The Sunshine Coast is one of Australia's fastest-growing urban regions and is renowned for its diverse coastal environments, including extensive wetlands, and estuarine system [17]. The Maroochy river estuary experiences significant pressure due to urbanization and broader climate impacts. It recorded declines in mangrove forests due to human activity from 1988 through to 2016 [18] but remains an enclave of biodiversity, providing habitat for shorebirds [19] and areas of supratidal wetlands, which continue to support a variety of plant species [20,21]. The region accommodates a blend of residential, tourism, and conservation land uses, with coastal ecosystems, which comprise mangroves, saltmarshes, and wetlands. These coastal environments provide essential ecological services, which include flood mitigation, biodiversity support, and blue carbon storage. Given the region's rapid urbanization and heightened exposure to climate-related issues, the Sunshine Coast is a strategically important site for examining sea-level trends, wetland dynamics and coastal vulnerability.

It is clear that in order to effectively address the challenge of more extreme storm and tidal events with rising sea levels, more accurate and efficient studies are needed that can support climate risk assessments and adaptation plans for coastal communities. The application of machine learning and deep learning technologies to monitor natural ecosystems is increasingly recognized as effective so as to provide accurate information for environmental scientists, planners and policy makers [22], yet at this stage, it is an emerging area of research. A 2025 comprehensive review of multidisciplinary studies that integrated machine learning with remote sensing technologies for water quality monitoring and prediction [22] identified only 186 journal articles. The majority of these (15 articles) were published in this journal, *Remote Sensing*, with just over 23% of the 186 articles applied to studies in environmental science. Landsat imagery provided by the United States Geological Survey (USGS) was the most common source of remote sensing data for monitoring water bodies, whilst the Sentinel 2 data provided by Copernicus Data Space Ecosystem were most commonly used for land, atmospheric and oceanic monitoring [22]. In regard to machine learning methods frequently employed in the review undertaken by [22], the Support Vector model was identified as a highly successful and well-established supervised machine learning model. Random forest was also identified as a popular ensemble-based supervised machine learning model, whilst the use of boosting algorithms, such as gradient boosting, were also identified as a common method used to increase the accuracy of weak learners [22]. The 2025 review also considered the use of deep learning models identifying Convolutional Neural Network (CNN) [23], and Long Short-Term Memory (LSTM) as one of the most widely used techniques in water quality applications [22].

An earlier review of studies centered on remote sensing and machine learning methods applied to the topic of invasive plants was published in 2024, in the journal of Remote Sensing [24]. The review identified the use of aerial photography using LiDAR data, and multispectral and hyperspectral images as complementary with other satellite derived remote sensing data to monitor vegetation changes, specifically the spread of invasive species. The use of deep learning models, ref. [24] contend has become increasingly dominant in the last ten years. CNN methods in addition to Deep Convolutional Neural Network (DCNN) and Generative Adversarial Network (GAN) were the most commonly employed methods featured in this review [24].

Of relevance to this study which focusses on monitoring and predicting the impact of sea-level rise and tidal surge on coastal wetlands, is a study undertaken in 2022 that used small unmanned aerial systems (sUAS) and deep learning technologies (U-net classifier) to monitor and model tidal marsh vegetation in South Carolina [25]. The study revealed insights into marsh health and land use changes due to coastal development. Other relevant studies concentrate on the use of remote sensing to map and monitor mangrove ecosystems,

one of which [26] recommends the use of deep machine learning which use both pixel-based and object-based approaches. Similarly, a 2024 review of studies that utilized remote sensing and geographic information systems to monitor coastline dynamics, noted that machine learning techniques were effective in extracting geomorphological data and in classifying coastal geomorphology [27].

This study extends knowledge related to the integration of deep machine learning technologies with remote sensing data to monitor wetland change and to project future changes. Specific references to other studies and techniques considered in this study is documented and presented in the comprehensive methods section below. The study proposes a hybrid deep learning Convolutional Neural Network—Bidirectional Long Short-Term Memory (CNNBiLSTM) model and remote sensing to predict maximum sea level (Hmax) and high tidal events in Maroochydore. In addition to this, the study also uses Landsat data for wetland change detection along Maroochy River floodplain and mean annual Hmax trend from 2014 to 2024. These techniques are tailored to specifically examine the encroachment on wetlands in this case study area.

The remainder of this paper is organized as follows: Section 2 describes the study area, dataset, preprocessing steps, theoretical background of models, evaluation metrics and flowchart summary. Section 3 presents the results and discussion which include the model evaluation results, result visualizations, tidal wave analysis, wetland change detection and Hmax trend. Section 4 concludes the paper with a summary and potential directions for future work.

2. Materials and Methods

2.1. Study Area and Dataset

The study focusses on a study site located within Maroochydore in Queensland, Australia. Figure 1 below illustrates the location on the map. Maroochydore is a coastal urban center situated within the Sunshine Coast region adjacent to the Coral Sea. The region is characterized by sandy beaches and estuarine systems. This study specifically targets the Maroochy River floodplain which lies within the coastal zone and features flat topography. This coastal area lies within a low-lying floodplain adjacent to the Coral Sea, making it highly vulnerable to the impacts of sea-level rise, storm surges, and tidal inundation.

The dataset for maximum sea level and associated oceanic parameters in this study is obtained from Queensland Government's Open Portal (Coastal Data System—Near real time storm tide data—Dataset—Open Data Portal | Queensland Government; https://www.data.qld.gov.au/dataset/coastal-data-system-near-real-time-storm-tide-data, accessed on 5 January 2024). The floating buoys record and transmit wave parameters to the receiver station which electronically processes and stores the dataset. The dataset for the Maroochy River floodplain wetland was derived from the National Aeronautics and Space Administration (NASA) Landsat mission (https://landsat.gsfc.nasa.gov/data/ (accessed on 5 January 2024)) for wetland satellite images from Collection 2 Tier 1 calibrated top-of-atmosphere (TOA) reflectance of the United States Geological Survey (USGS) Landsat 7 and 8 image at a 30-m digital elevation. Table 1 outlines the oceanic parameters obtained via Queensland Open Portal site for maximum sea level forecasting in this study. Zero up crossing wave period (Tz) is the time (in seconds) interval between two successive points where the wave elevation crosses the mean water level (typically zero) in the upward direction [28]. Peak energy wave period (Tp) is the wave period (in seconds) corresponding to the frequency at which the wave energy spectrum reaches its maximum [29]. Sea surface temperature (°C) is the temperature of the uppermost layer of the ocean, typically measured at or near the surface [30]. A lag in time series analysis refers to the time difference between a current data point and a previous data point used for comparison. When working with

60-min (hourly) data as in this study, a lag of 5 corresponds to the value recorded 5 h before the current time t. Specifically, lag 1 (L1) is the value at time (t − 1), (one hour ago), lag 2 (L2) is at (t − 2) (two hours ago), lag 3 (L3) at (t − 3), and so forth up to lag 5 (L5), which is the value at time (t − 5) (five hours ago). These lagged values help identify relationships and dependencies across time within the data, making them useful in forecasting, autocorrelation, and modelling how past values influence current or future observations In signal processing and decomposition methods like Successive Variational Mode Decomposition (SVMD), a successive mode refers to each component or Intrinsic Mode Function (IMF) extracted one after another in sequence from the original signal. [31]. Each IMF (in metres) represents a simple oscillatory mode embedded in the original data, with well-defined instantaneous frequencies. When a signal is decomposed into 3 IMFs, the original time series is separated into three different oscillatory components, each capturing different frequency bands or patterns within the data. IMF 1 corresponds to the highest-frequency oscillations (fastest fluctuations), IMF 2 captures medium-frequency oscillations, and IMF 3 represents lower-frequency trends or slower variations. Analysing these IMFs individually allows for better understanding and interpretation of the underlying processes at different time scales within the original signal.

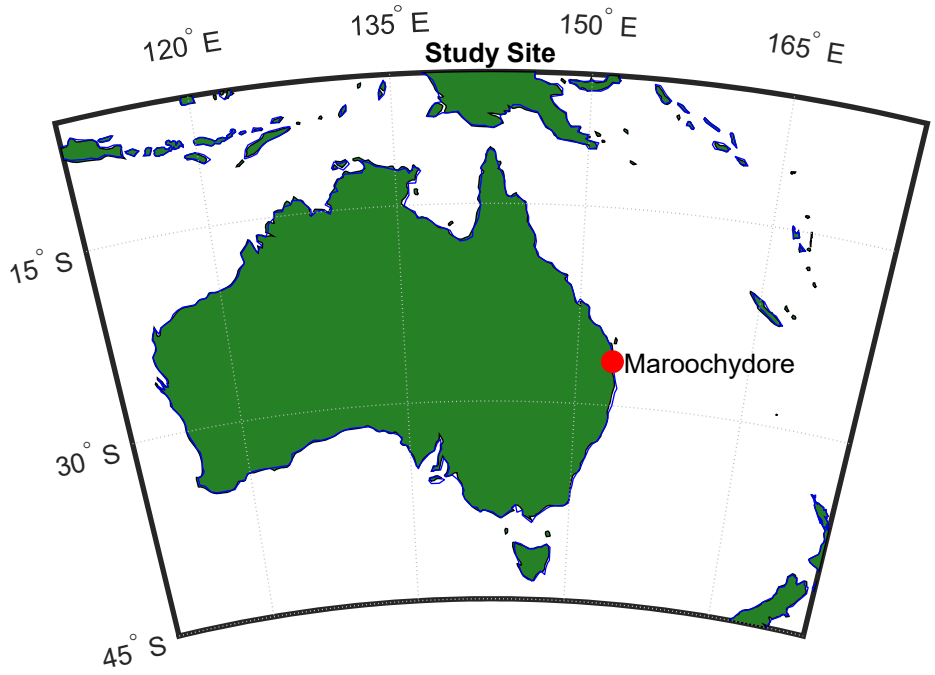

Figure 1. Study site map of Australia showing the geographical location of Maroochydore in Queensland, Australia.

Table 1. The oceanic parameters utilized for modeling in the study.

Input Wave Features	Description
Hmax	Maximum sea level (m)
Tz	Zero up crossing wave period (s)
Tp	Peak energy wave period (s)
SST	Sea surface temperature (°C)
(t − 1) (t − 2) (t − 3) (t − 4) (t − 5)	Hmax Lags (m)
IMF1, IMF2, IMF3	Intrinsic Mode Functions (IMFs) (m)

2.2. Data Preprocessing and Model Inputs

Data preprocessing is a critical step in the development of robust and reliable data models [32]. The accuracy and efficiency of artificial intelligence (AI) models are highly dependent on the quality of input data, as well as the selection of relevant features that guide the model's learning and prediction processes. To capture temporal dependencies and allow the models to detect repeating patterns, lags are an important input in the AI-based modelling [33]. It is important to understand historical data in predicting of future changes [34]. Statistical tools such as Autocorrelation function (ACF) and Partial Autocorrelation function (PACF) are widely used to determine how a sea level time series data is correlated to its past values [35,36]. Figure 2 presents the results of the ACF and PACF analysis, highlighting the significant lags that were used as model inputs. To investigate the inputs with sea level dataset parameters and lags, correlation of the inputs were computed as shown in Table 2. It is important to see the inter dependent realtionship of the target variable with other oceanic variables for modeling [37]. Table 2 displays the strength of the relationship of Hmax with all inputs with colour and darker shades imply a stronger correlation.

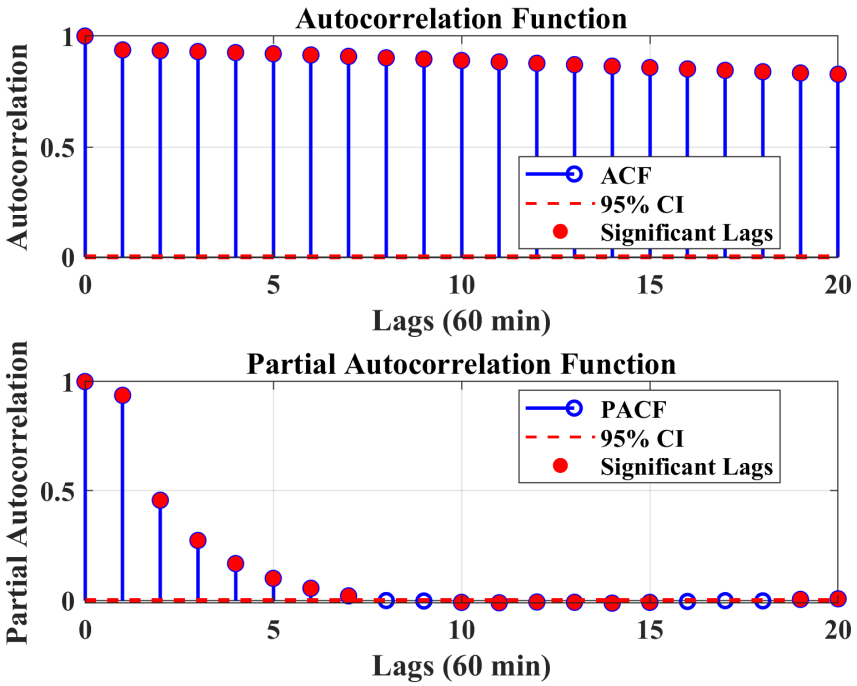

Figure 2. ACF and PACF lags of Hmax sea level data for Maroochydore Sea level tide gauge in Queensland, Australia.

Table 2. Maximum Sea Level (Hmax) Correlation with Observed Oceanic Parameters and Lags.

	Tz	Tp	SST	L1	L2	L3	L4	L5	Hmax
Tz	1.0000	0.4877	0.0445	0.3381	0.3333	0.3285	0.3239	0.3194	0.3475
Tp	0.4877	1.0000	−0.0867	−0.0108	−0.0119	−0.0126	−0.0124	−0.0122	−0.0082
SST	0.0445	−0.0867	1.0000	0.2176	0.2181	0.2185	0.2191	0.2197	0.2173
L1	0.3381	−0.0108	0.2176	1.0000	0.9375	0.9341	0.9301	0.9254	0.9375
L2	0.3333	−0.0119	0.2181	0.9375	1.0000	0.9375	0.9341	0.9301	0.9341
L3	0.3285	−0.0126	0.2185	0.9341	0.9375	1.0000	0.9375	0.9341	0.9301
L4	0.3239	−0.0124	0.2191	0.9301	0.9341	0.9375	1.0000	0.9375	0.9254
Hmax	0.3475	−0.0082	0.2173	0.9375	0.9341	0.9301	0.9254	0.9202	1.0000

2.3. Data Decomposition

Data decomposition is an effective technique to improve the prediction of AI models in many studies [38–40]. These methods decompose and extract useful information at different frequencies [40,41]. In this study, the Successive Variational Mode Decomposition (SVMD) [42] was employed, which is a powerful technique for concurrently decomposing a signal into its constituent intrinsic modes. Successive Variational Mode Decomposition (SVMD) is a method that extracts modes one at a time without requiring prior knowledge of how many modes are present. Like VMD, it treats each mode as a signal with the most compact spectrum. However, SVMD modifies the VMD optimization problem by introducing additional criteria [42]. The extracted mode should have minimal or no spectral overlap with the remaining modes or the residual signal. Furthermore, SVMD has significantly lower computational complexity and offers greater robustness to the choice of initial center frequencies compared to VMD [42]. SVMD is an improved version of Variational Mode Decomposition (VMD) where the performance is not affected if the number of modes in the signal is not precisely known [42]. Decomposition of the signal is done by successively applying Variational Mode Extraction (VME) which extracts the intrinsic mode function by its approximate center frequency. Unlike VMD which extracts modes concurrently, SVMD extracts the modes in a successive manner which reduces complexity [42,43]. SVMD breaks down complex non stationary signals into its IMFs and addresses the issue of mode mixing better when compared to EMD, EEMD and CEEMDAN [43]. The sea level data contains trends, seasonal cycles, tidal oscillations and extreme events hence decomposition techniques help to break these into simpler oscillatory modes for AI modelling [38,41]. The resulting IMFs shown in Figure 3 capture the local characteristics of the original signal and represent intrinsic modes of oscillation that reflect the maximum sea level signal variability in maximum sea level (Hmax).

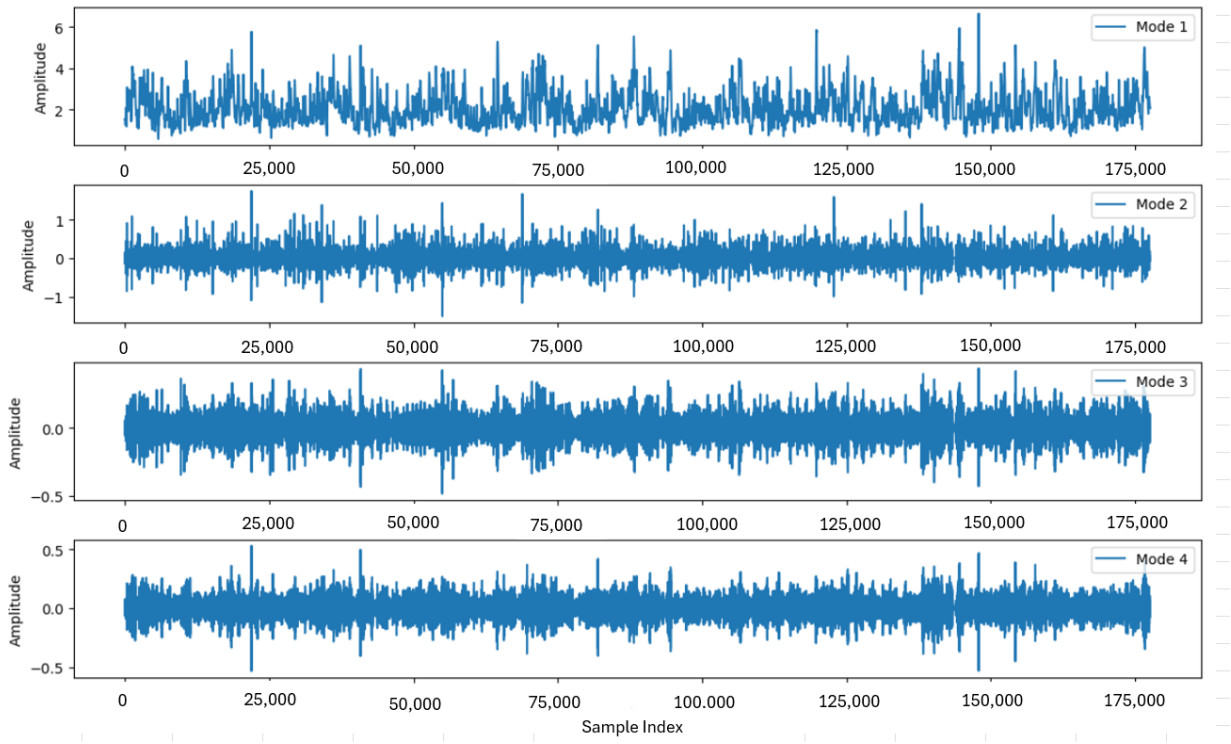

Figure 3. Decomposed Maximum Sea Level (Hmax) IMFs obtained from SVMD decomposition for the Maroochydore Tide Gauge study site.

2.4. Data Normalization

The final step of data preprocessing before feeding the dataset for data partition in AI modelling is normalization using the Equation (1) given below:

$$x_n = \frac{x_{\text{actual}} - x_{\text{min}}}{x_{\text{max}} - x_{\text{min}}} \quad (1)$$

Normalization of large values of the dataset helps to reduce the time taken for the learning stage in AI modelling [44]. Neural networks which rely on gradient based architecture tend to converge faster when features are within the same scale [45]. The values are converted back to normal using Equation (2) below after prediction.

$$x_{\text{actual}} = x_n(x_{\text{max}} - x_{\text{min}}) + x_{\text{min}} \quad (2)$$

2.5. Data Partition

The partition of dataset into training, validation and testing is an important step to ensure data is divided to build, tune and evaluate the models effectively. Each set is important and distinct so that overfitting, underfitting and overlap is avoided [46].There is no set rule for the partition and this study aligns with other studies [40,47,48] which divide the dataset into 60% for training, 20% for validation and 20% for testing as shown in Table 3 below.

Table 3. Data partition breakdown with dates for the study sites.

Partition	Training (60%)	Validation (20%)	Testing (20%)
Oceanic Dataset	January 2014–December 2019	January 2020–December 2021	January 2022–December 2023

2.6. Objective Model Theoretical Background: Convolutional Neural Network-Bidirectional Long Short-Term Memory (CNNBiLSTM)

This study uses a hybrid CNNBiLSTM as the objective model for predicting Hmax in Maroochydore. This helps to take advantage of CNN and BilSTM layers in feature extraction and learning for prediction. The 1-dimensional CNN uses specialized layers to process sequential time series data [49]. The core layers apply one dimensional convolution and filters on the input dataset. The pooling layer reduces the dimensionality and the flatten layer converts the output into a one dimensional vector [50]. The Bidirectional Long Short-Term Memory (BiLSTM) model architecture consists of two Long Short-Term Memory (LSTM) networks. Long Short-Term Memory (LSTM) neural networks are a special type of Recurrent Neural Network (RNN) which is designed to learn long term dependencies on sequential dataset [51]. LSTM networks are comprised of three layers: an input layer, one or more hidden layer(s), and an output layer, with the neuron number in the input/output layer equivalent to the amount of feature space [52]. Memory cell(s) within these hidden layers have three gates: forget, input, and output, and at every time-step t, each gate is presented with an input x_t and the output of the memory cells at the previous time step, x_{t-1}. For each time-step, the cell state s_t and output h_t is calculated and the gates act as filters. The forget gate determines what information will be removed from the cell state and the input gate selects what new information should be added. The output gate decides which part of the cell state should be passed on as the output [53]. The gates and functions below form the basis of the overall architecture (see Figure 4):

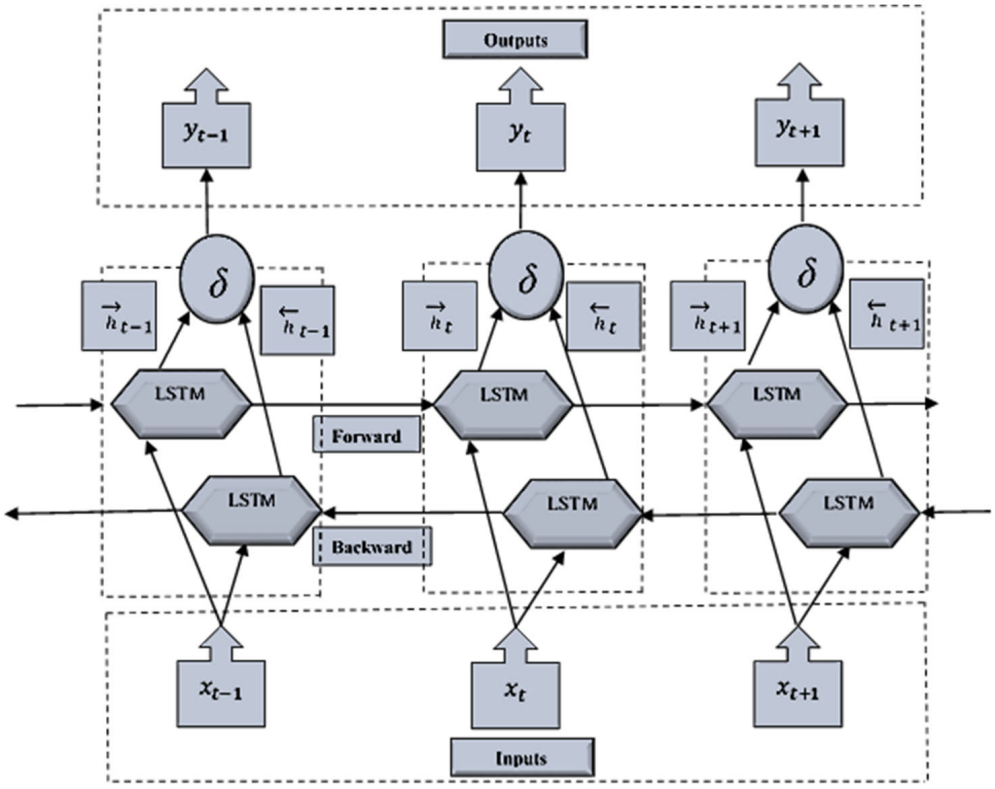

Figure 4. The BiLSTM cell structure at time step t. The architecture has the forward and backward flow arrangement of connected LSTM layers.

Forget Gates:

$$f_t = \delta_g\left(W_f x_t + U_f h_{t-1} + b_f\right) \tag{3}$$

Input Gates:

$$i_t = \delta_g(W_i x_t + U_i h_{t-1} + b_i) \tag{4}$$

Output Gates:

$$o_t = \delta_g(W_o x_t + U_o h_{t-1} + b_o) \tag{5}$$

Sigmoid Function:

$$\delta_g(x) = \frac{1}{1 + e^{-x}} \tag{6}$$

Cell Input State:

$$\check{c}_t = tanh(W_c x_t + U_c h_{t-1} + b_c) \tag{7}$$

Hypertangent Function:

$$tanh(x) = \frac{e^x - e^{-x}}{e^x + e^{-x}} \tag{8}$$

where, b_f, b_i , b_o and b_c are bias vectors. The U_f, U_i, U_o, and U_c are weight matrices connecting the previous cell output state to the gates and the input cell state. The W_f, W_i, W_o, and W_c are weight matrices that maps the hidden layer input to the gates and the input cell state. The gate activation function δ_g used in this modelling process is sigmoid. The cell output c_t and output h_t at each iteration t are as follows:

$$c_t = f_t * c_{t-1} + i_t * \check{c}_t \tag{9}$$

$$h_t = o_t * \tanh(c_t) \tag{10}$$

The input is processed in both directions with separate hidden layers as shown in Figure 4. Final output is given as:

$$Y_t = [\ldots, y_{t-1}, y_t, y_{t+1}, \ldots]. \tag{11}$$

The architecture used Adam optimizer for training as shown in Table 4. It is efficient in adaptive learning rate and performance on a wide range of large datasets [54]. Rectified Linear Unit (ReLU) is employed as the activation function which helps in faster convergence and mitigation of the vanishing gradient issue [55]. For weight regularization, an L2 penalty of 0.01 is applied (with L1 set to 0), which helps to prevent overfitting by discouraging large weights. A dropout rate of 0.1 is chosen from grid search, randomly deactivating 10% of the neurons during training to further enhance generalization. To optimize training and avoid overfitting, early stopping is implemented with a mode set to 'minimum' and a patience of 20 epochs [56]. This will ensure that training will stop if the validation loss does not improve for 20 consecutive epochs. Figure 5 shows a snapshot of model summary with engaged layers, output shape and parameters. Figure 6 shows the data flow for training, validation and prediction with relevant hyperparameters.

Table 4. BiLSTM model variables and hyperparameters obtained from Grid Search in Python 3.12.3.

Optimizer	Activation Function	Weight Regularization	Dropout	Early Stopping
Adam	Rectified Linear Unit (ReLU)	L1 = 0, L2 = 0.01	0.1	Mode = Minimum, Patience = 20

```
_________________________________________________
 Layer (type)                Output Shape
=================================================
 conv1d (Conv1D)             (None, 8, 5)

 bidirectional (Bidirectiona  (None, 8, 20)
 l)

 flatten (Flatten)           (None, 160)

 dense (Dense)               (None, 64)

 dense_1 (Dense)             (None, 1)

=================================================
Total params: 14,544
Trainable params: 14,544
Non-trainable params: 0
```

Figure 5. A snapshot within the BiLSTM model development phase.

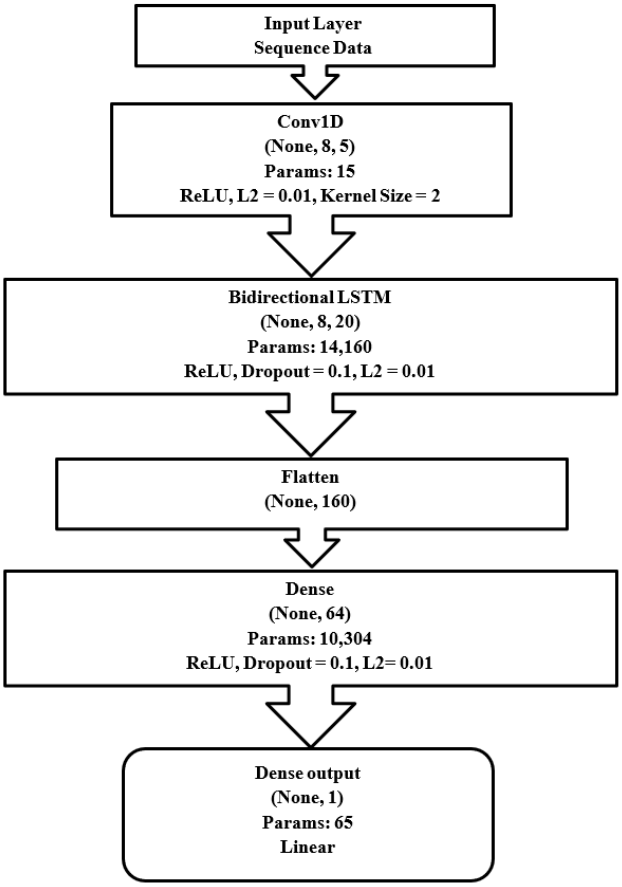

Figure 6. Model Layers showing the data flow for training, validation and prediction in the network with the hyperparameters.

2.7. Benchmark Models: Theoretical Background

2.7.1. Multilinear Regression (MLR)

Multiple Linear Regression (MLR) is a mathematical model that estimate the relationship between two or more explanatory variables and one response variable [57]. The MLR model is a supervised learning algorithm which can be used to predict a target variable with given multiple input variables.

The formula for MLR is:

$$y = \beta_0 + \beta_1 X_1 + \beta_2 X_2 + \ldots + \beta_n X_n + \epsilon \quad (12)$$

where y is the predicted or expected value of the dependent variable, β_0 is the y-intercept (i.e., the value of y when all other parameters are set to 0), β_1 to β_n are the regression coefficients of the independent variables X_1 to X_n and ϵ is the model error that measures how much variation exists in the estimate of y [58].

2.7.2. Support Vector Regression (SVR)

Vapnik and colleagues proposed the Support Vector (SV) algorithm [59] based on non-linear generalisation of the generalised portrait algorithm [59,60]. The Support Vector Machine (SVM) was adapted for regression tasks, resulting in the Support Vector Regression (SVR) model. It is based on the same underlying principles but work effectively with time series numerical dataset [58,61]. This regression version was developed by Vapnik, Steven Golowich, and Alex Smola in 1997 [62]. SVR is used for prediction to minimize error, identify the optimal solution, and mitigate the effects of the "curse of dimensionality," [63]. The model constructs a linear function:

$$f(x) = w^T x + b \tag{13}$$

The weight vector w and bias b are optimized to minimize the model complexity, represented by $\frac{1}{2} \parallel w \parallel^2$ and the prediction error beyond the ε margin [64].

2.7.3. Categorical Boosting (CatBoost)

CatBoost is from the family of Gradient Boosted Decision Trees (GBDT's) machine learning techniques [65]. The algorithm was proposed in [66] and can be effectively used to solve problems with heterogeneous features, noisy data and complex dependencies [67].

CatBoost models an unknown function to build an ensemble of decision trees. The predicted output is given by $\hat{y}$:

$$\hat{y} = \sum_{m=1}^{M} \eta \cdot T_m(x) \tag{14}$$

Each component plays a critical role in the learning process. M denotes the total number of trees or boosting iterations used in the ensemble. The learning rate η controls the contribution of each individual tree to the final prediction, thereby balancing learning speed and model accuracy [68]. $T_m(x)$ represents the output of the m^{th} decision tree given the input features x with each tree trained to correct the residual errors of the previous ones.

2.8. The Performance Evaluation Metrics for AI Models

The models were evaluated based on the testing dataset using ten statistical metrics (four classification) from Equations (15)–(27) of the predicted results. The models were evaluated by comparing the model predictions. These metrics provide insights into the accuracy, reliability, and agreement between predicted and observed values. Pearson Correlation Coefficient (r) measures the strength and direction of the linear relationship between predicted and observed values. Values near +1 or −1 indicate strong correlation, while values near 0 suggest little to no linear relationship [69]. Coefficient of determination (R^2) is a statistical measure that shows how well a regression model explains the variability of the target variable [70]. It represents the proportion of the total variation between the observed and predicted data and is used in the scatterplots in visualization of results. Willmott's Index of Agreement (d) evaluates the degree to which predicted values match the observed values, accounting for both systematic and random errors. It ranges from 0 (no agreement) to 1 (perfect agreement) [71]. Nash-Sutcliffe (NS) Coefficient assesses the predictive skill of the model by comparing it to the mean of the observed data. A high NS value indicates that the model performs well relative to simply using the mean as a predictor [72]. Legates and McCabe's Efficiency Index (LM) is a modified version of NSE that uses absolute errors rather than squared errors, making it more robust to outliers. It is particularly useful in environmental modeling where extreme values can skew traditional metrics [47].

In addition to performance metrics, error metrics also help to evaluate the efficiency of AI models. Mean Absolute Error (MAE) represents the average absolute difference between predicted and actual values [70]. Mean Absolute Percentage Error (MAPE) gives the average absolute error as a percentage of the actual values. This helps to provide a normalized measure of prediction accuracy [73]. Root Mean Squared Error (RMSE) measures the average magnitude of the prediction errors [74]. It is the square root of the Mean Squared Error (MSE) and is expressed in the same units as the target variable. A confusion matrix is a tabular representation of the actual versus predicted classifications [75]. In binary classifications, accuracy is the ratio of correctly predicted to the total observations. Precision measures the proportion of correctly predicted positive cases out of all cases

predicted as positive. Recall quantifies the ability of the model to identify all relevant positive cases. The F1 score is the harmonic mean of precision and recall.

1. Pearson Correlation Coefficient (r)

$$r = \left[\frac{\sum_{i=1}^{n}(DO_i - MDO)(DS_i - MDS)}{\sqrt{\sum_{i=1}^{n}(DO_i - MDO)^2 \sum_{i=1}^{n}(DS_i - MDS)^2}} \right]^2 \tag{15}$$

2. Coefficient of Determination (R^2)

$$R^2 = 1 - \frac{\sum(y_i - \hat{y}_i)^2}{\sum(y_i - \overline{y})^2} \tag{16}$$

3. Willmott's Index of Agreement (d)

$$d = 1 - \left[\frac{\sum_{i=1}^{n}(DO_i - DS_i)^2}{\sum_{i=1}^{n}(|DS_i - MDO| + |DO_i - MDS|)^2} \right] \tag{17}$$

4. Nash-Sutcliffe Coefficient (NS)

$$NS = 1 - \left[\frac{\sum_{i=1}^{n}(DO_i - DS_i)^2}{\sum_{i=1}^{n}(DO_i - MDO)^2} \right], -\infty \leq NS \leq 1 \tag{18}$$

5. Legates and McCabe's Index (LM)

$$LM = 1 - \left[\frac{\sum_{i=1}^{n}|(DS_i - DO_i)|}{\sum_{i=1}^{n}|DO_i - MDS|} \right], \ 0 \leq L \leq 1 \tag{19}$$

6. Root Mean Square Error ($RMSE$)

$$RMSE = \sqrt{\left(\frac{1}{n}\right) \sum_{i=1}^{n}(DS_i - DO_i)^2} \tag{20}$$

7. Mean Absolute Error (MAE)

$$MAE = \frac{1}{n} \sum_{i=1}^{n}|(DS_i - DO_i)| \tag{21}$$

8. Mean Absolute Percentage Error ($MAPE$)

$$MAPE = \frac{1}{\mathrm{N}} \left(\sum_{N}^{i=1} \left| \frac{(SWL_{for} - SWL_{obs})}{SWL_{obs}} \right| \right) \times 100 \tag{22}$$

9. Confusion Matrix (CM)

$$CM = \frac{\sum_{i=1}^{C} M_{i,i}}{\sum_{i=1}^{C} \sum_{j=1}^{C} M_{i,j}} \tag{23}$$

$$\sum_{\mathrm{i=1}}^{\mathrm{C}} \mathrm{M}_{i,i} = \text{sum of diagonal elements (correct predictions)},$$

$$\sum_{\mathrm{i=1}}^{C} \sum_{\mathrm{j=1}}^{C} \mathrm{M}_{i,j} = \text{total number of predictions.}$$

10. Classification:

$$Accuracy = \frac{TP + TN}{TP + TN + FP + FN} \tag{24}$$

$$Precision = \frac{TP}{TP + FP} \tag{25}$$

$$Recall = \frac{TP}{TP + FN} \tag{26}$$

$$F1\ Score = 2 \times \frac{Precision \times Recall}{Precision + Recall} \tag{27}$$

$$\text{TP} = \text{True Positive},\ \text{TN} = \text{True Negative},$$

$$\text{FN} = \text{False negative},\ \text{FN} = \text{False negative}$$

2.9. Flowchart Summary of Hmax Forecasting

Figure 7 illustrates the process of Hmax forecasting using the oceanic dataset. The data preprocessing is the initial stage to clean and fill in any missing values using data interpolation. This is followed by the computation of Hmax lags (from t − 1 to t − 5) and data normalization. In time series analysis, lags are created by shifting a variable's value backward in time to represent its past states as additional input features for a predictive model [76]. The next step involves correlation analysis to identify significant features for model inputs. The refined dataset undergoes data decomposition using SVMD (Successive Variational Mode Decomposition) to extract intrinsic mode functions (IMF1, IMF2, and IMF3). These decomposed components, along with input features such as Tp, Tz, SST, Hs, and lagged values of Hmax (from t − 1 to t − 5), are used to predict the target variable (Hmax). Four models are employed for prediction: CatBoost, MLR (Multiple Linear Regression), SVR (Support Vector Regression), and a hybrid CNN-BiLSTM model. The outputs from these models are then passed through a denormalization step to revert the data to its original scale, resulting in the final forecasted Hmax value.

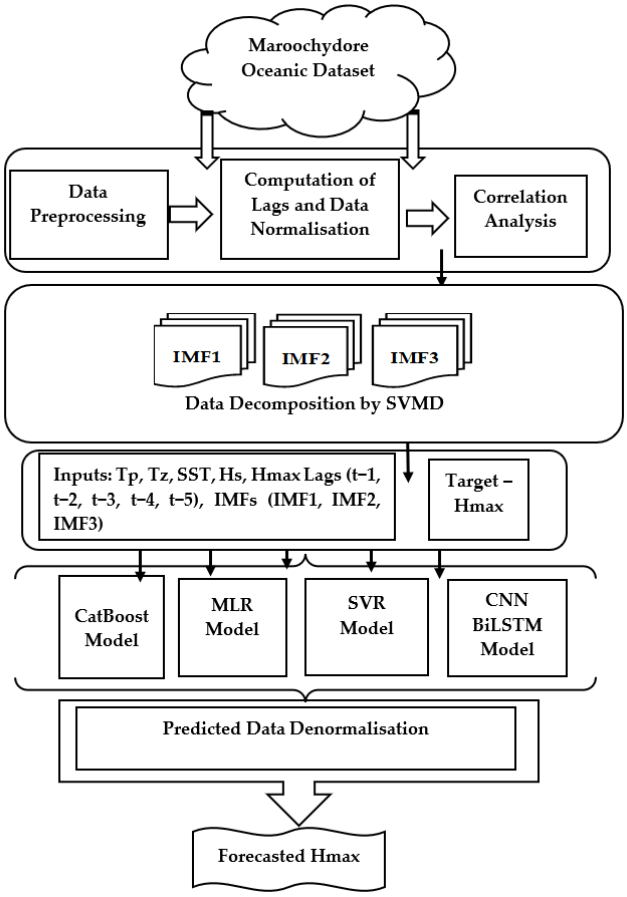

Figure 7. Flowchart summary of Hmax forecasting.

3. Results and Discussion

3.1. Model Evaluation Results

Table 5 below shows the results of evaluation metrics for Hmax prediction. Among the models evaluated, the CNNBiLSTM model clearly outperforms all the benchmark models across all metrics. It achieves the lowest MAE (0.1472), MSE (0.0438), RMSE (0.2092), and MAPE (6.8829%), while also attaining the highest R^2 score (0.9503), Pearson correlation coefficient (r = 0.9748), Wilmott index (0.9867), Nash-Sutcliffe efficiency (0.9492), and Legates-McCabe index (0.7942). In contrast, SVR shows the weakest performance with significantly higher error metrics and lower efficiency indicators. Meanwhile, CatBoost and MLR demonstrated moderately strong performances, with very low error and high efficiency scores. This comparison highlights the advantage of implementing a hybrid deep learning framework for capturing complex patterns in sea level data.

Table 5. Model performance and error metrics for Hmax prediction.

Model	MAE	RMSE	MAPE (%)	R^2	r	Wilmott	Nash Sutcliffe	Legates McCabe
CNNBiLSTM	0.1472	0.2092	6.8829	0.9503	0.9748	0.9867	0.9492	0.7942
CatBoost	0.1943	0.2725	9.2743	0.9139	0.9560	0.9768	0.9138	0.7284
MLR	0.1961	0.2746	9.3755	0.9125	0.9552	0.9765	0.9125	0.7259
SVR	0.3371	0.3925	20.6861	0.9098	0.9538	0.9485	0.8212	0.5288

3.2. Result Visualizations and Discussion

Figure 8 shows the scatterplot of observed versus predicted data. The closely packed cluster of points indicate the higher accuracy of the models. CNNBiLSTM shows most of the points are clustered together around the line of best fit with highest R^2 value for the Hmax study site. Scatterplots also reveal a general pattern between the observed and predicted data points. Figure 9 shows the absolute prediction error distribution for all models. This is a helpful tool to understand how models can have small or large errors between observed and predicted values [38]. The bars closer towards the lower end as in CNNBiLSTM indicates higher accuracy. Figure 8 illustrates the time series trend of 100 data points, highlighting the close alignment between observed and predicted values. The minimal deviation between the two line curves visually supports the accuracy of the CNNBiLSTM model prediction. As shown in Figure 10, benchmark models show the greater presence of outliers that associate with lower accuracy [77].

3.3. Wetland Detection Results

In this study, Google Earth Engine (GEE) and QGIS was utilized to assess wetland changes by analysing surface reflectance data from USGS Landsat Tier 1 Surface Reflectance imagery dataset. Landsat 5 was selected for the year 2009, while Landsat 8 imagery was used for 2023, with both datasets filtered to reduce cloud cover and clipped to the Maroochydore River Floodplain defined Region of Interest (ROI) as shown in Figures 11 and 12. The study used six indices from surface reflectance bands of Landsat imagery. These included Normalized Difference Vegetation Index (NDVI), Normalized Difference Water Index (NDWI), Modified NDWI (MNDWI) and Normalized Difference Moisture Index (NDMI). Each index was calculated using band specific normalised differences. Soil-Adjusted Vegetation Index (SAVI) and Enhanced Vegetation Index (EVI) were additionally derived for soil brightness and atmospheric effects. These were integrated into the original imagery and served as input features for the supervised classification. The Normalized Difference

Vegetation Index (NDVI) [78] was calculated for both years using the near-infrared and red bands to extract vegetation distribution and detect potential water presence. To complement NDVI, additional spectral indices were computed to enhance wetland detection accuracy. These included the Modified Normalized Difference Water Index (MNDWI) [79], which improves the delineation of open water and flooded areas; the Normalized Difference Moisture Index (NDMI) [80], which is sensitive to vegetation moisture content; and the Soil-Adjusted Vegetation Index (SAVI) [81], which accounts for soil background effects in sparse vegetation zones. The Enhanced Vegetation Index (EVI) [82] was also used to better capture canopy dynamics in densely vegetated wetlands. The difference in NDVI values between the two years was used to detect changes in vegetation cover. A threshold was applied to isolate significant NDVI changes, and the extent of change was quantified using pixel-based area calculations.

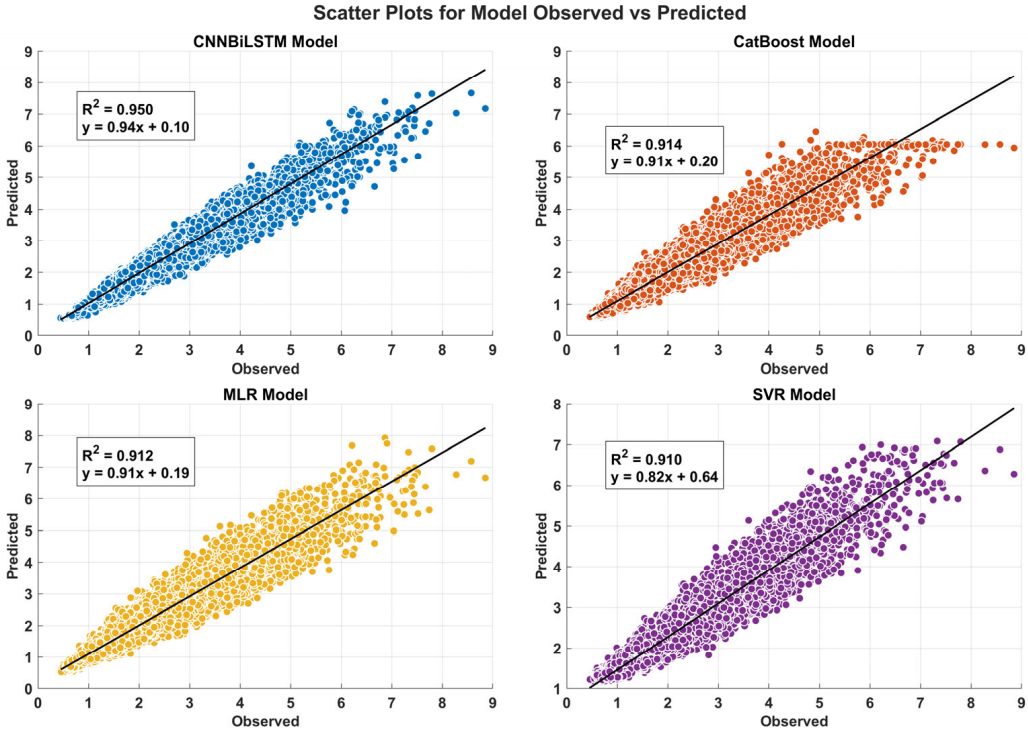

Figure 8. Scatter plot of predicted vs. observed Hmax. A least square regression line and coefficient of determination with a linear fit equation are shown in each sub-panel.

The change detection analysis focussed on three key classes of wetland, water and land. Ground truth labels were derived from the ESA WorldCover dataset, which is remapped into the three target classes and used to generate balanced training and validation samples. A random forest classifier is trained on the ground truth data and then applied to both 2015 and 2023 imagery to classify each pixel. The model's performance is evaluated using a confusion matrix for reporting overall accuracy and kappa coefficient for each class. Tables 6 and 7 below show the evaluation results.

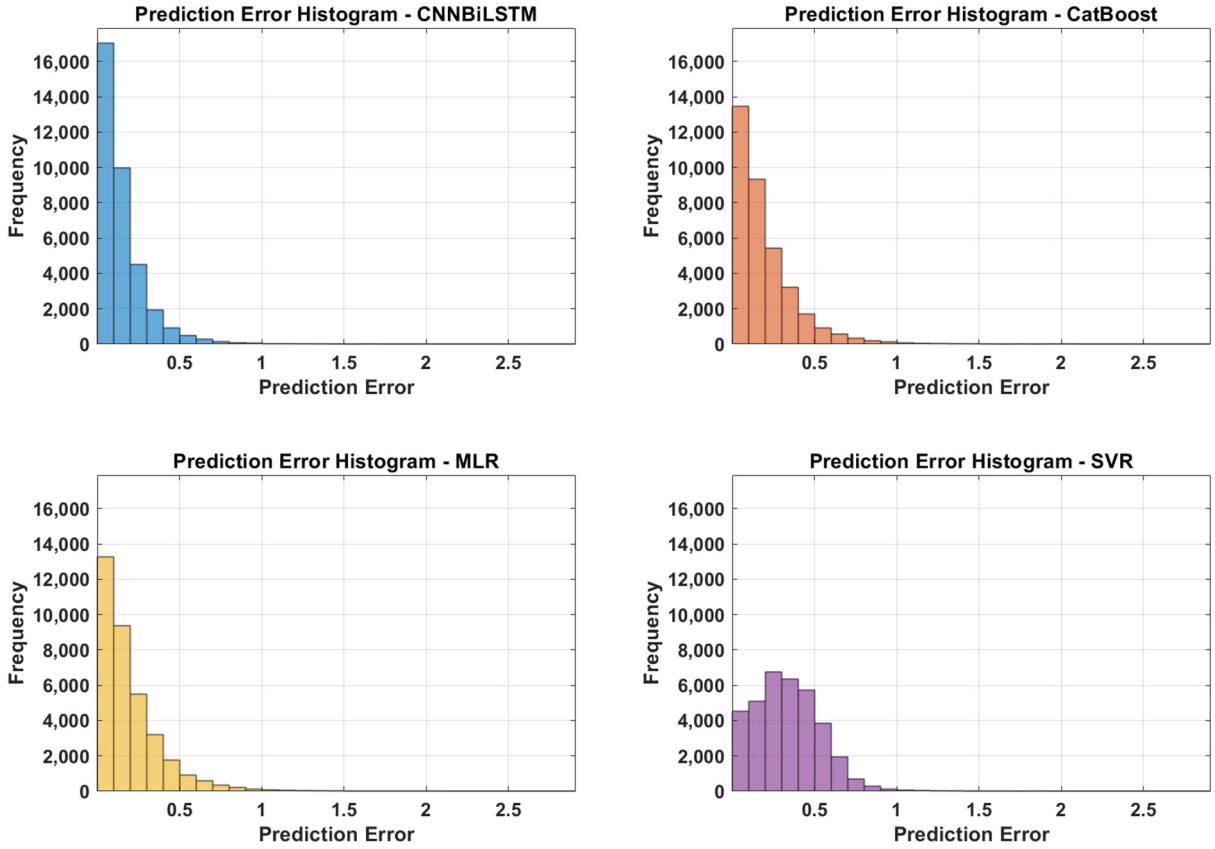

Figure 9. Histograms of absolute prediction error (PE) generated by CNNBiLSTM and the benchmark models.

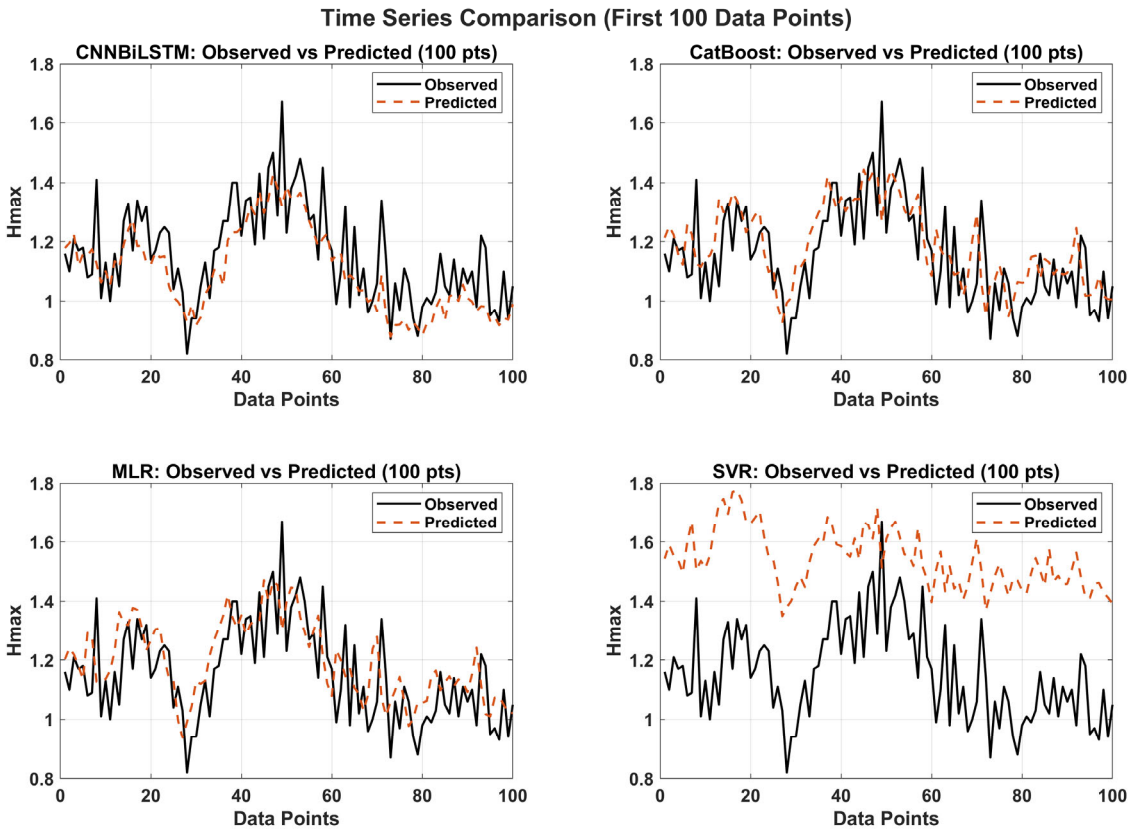

Figure 10. Time Series Comparison of CNNBiLSTM with the benchmark models.

Figure 11. 2009 Wetland vegetation extraction (in hectares (ha)) for Maroochy River floodplain study location derived from Landsat Surface Reflectance Tier 1 Imagery Dataset.

Figure 12. 2023 Wetland vegetation extraction (in hectares (ha)) for Maroochy River floodplain study location derived from Landsat Surface Reflectance Tier 1 Imagery Dataset.

Table 6. Wetland change detection classification and evaluation metrics.

Metric	Value	Description
Training Samples Count	1073	Number of points used to train the classifier
Validation Samples Count	427	Number of points used to test classifier accuracy
Confusion Matrix	[[131, 20, 1], [24, 109, 2], [0, 3, 137]]	Matrix comparing predicted vs actual classes (rows = actual, cols = predicted)
Overall Accuracy	0.8829	Fraction of correctly predicted validation samples
Kappa Coefficient	0.8241	Agreement with ground truth beyond chance
Recall	Land: 86.8 Wetland: 81.3 Water: 97.9	Proportion of true positive predictions among all the actual positive cases
Precision	Land: 84.5 Wetland: 81.3 Water: 97.1	Proportion of true positive predictions among all the predicted as positive

Table 7. Confusion matrix for wetland classification and ground truth evaluation.

	Predicted Land (0)	Predicted Wetland (1)	Predicted Water (2)
True Land (0)	131	20	1
True Wetland (1)	24	109	2
True Water (2)	0	3	137

This change detection identified the regions where wetland conditions had notably altered between 2009 and 2023. Table 8 shows results of the change detection with a decline of 395.64 hectares. This also aligns with a similar remote sensing study [18], which reported a decline in mangroves in the Maroochy River Floodplain of 583 hectares from a different timeline of 1988 to 2016. In addition to this, according to the 2021 Healthy Land Water Report 2021 [83], wetland extent in the Maroochy River remains poor in the inland freshwater reaches of the catchment. According to this report, the total wetland area in the Maroochy River catchment is around 8624 hectares. It includes various wetland types such as palustrine, riverine, and intertidal systems. The palustrine wetlands, which are freshwater wetlands like swamps and marshes, constitute about 3051 hectares, making them the most prevalent wetland type in the region. Riverine wetlands make up approximately 2346 hectares, while intertidal wetlands, including saltmarshes and mangroves, account for about 804 hectares. The decline and vegetation health awareness have led to efforts such as the Blue Heart project in the catchment, specifically targeting over 5000 hectares for restoration and conservation efforts [84].

Table 8. Wetland change detection from 2009 to 2023 for the Maroochy River Floodplain study site.

Wetland Vegetation Study Area	2009 Area	2023 Area	Detected Decline in Coastal Wetland Area from 2009 to 2023
Maroochy River Floodplain	2787.61 ha	2391.97 ha	395.64 ha

The Normalized Difference Vegetation Index (NDVI) is a widely used spectral index that indicates the presence and condition of live green vegetation [85]. It acts as a measure for vegetation productivity, health and growth [86]. It is calculated as follows:

$$\text{NDVI} = \frac{\text{NIR} - \text{RED}}{\text{NIR} + \text{RED}}, \tag{28}$$

where NIR represents the near-infrared band and RED refers to the red band of the electromagnetic spectrum. Healthy vegetation is indicated by a higher NDVI value since it reflects more NIR and absorbs more red light [86]. To further investigate the wetland vegetation in the study area, mean NDVI vales were calculated from 2015 to 2023, as shown in Figure 13.

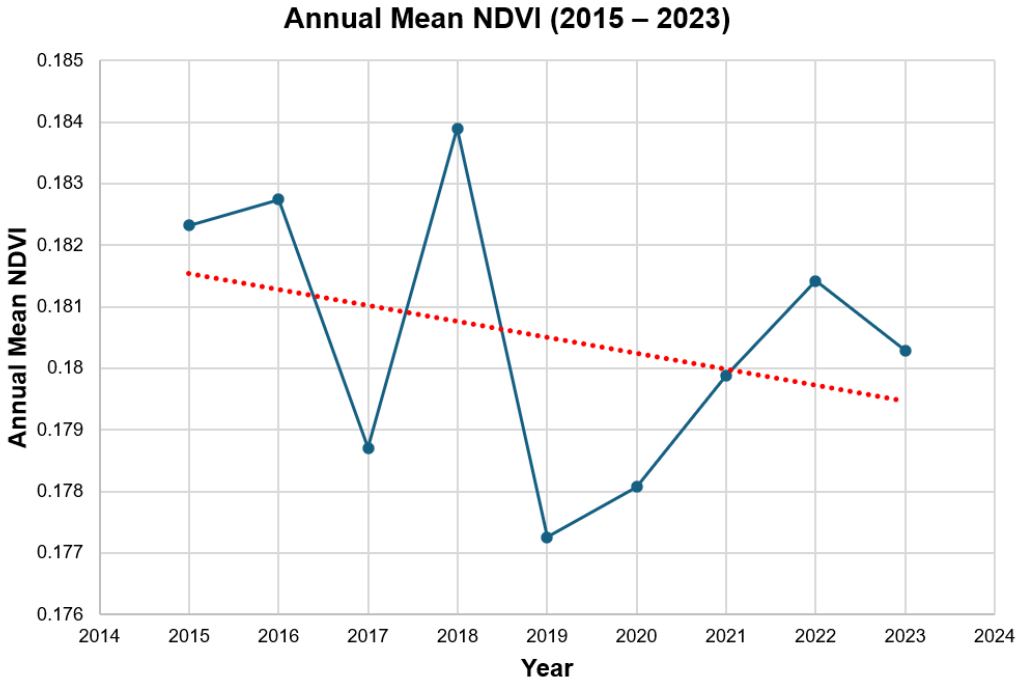

Figure 13. Wetland mean NDVI trend for Maroochy River Floodplain study location.

3.4. Wave Height Detection Results

The analysis for tidal wave height detection utilized a 30 min interval from 2014 to 2024 of maximum wave height, Hmax and the significant wave height Hs. To reduce noise and short-term variability, Hmax is smoothed using a moving centered average over a window size of w:

$$\widetilde{H}_{max}(t) = \frac{1}{w} \sum_{i=t-k}^{t+k} H_{max}(i), \tag{29}$$

where t is time and $k = \frac{w-1}{2}$.

The tidal wave threshold Th_w is defined using the 99th percentile of Hs:

$$Th_w = P_{99}(H_s). \tag{30}$$

The detection is based on the following condition:

$$\text{Detected Tidal Wave}: \ \widetilde{H}_{max}(t) > Th_w. \tag{31}$$

These peak values represent significant tidal occurrences affecting the Maroochydore coastline. The detected peaks are shown in Figure 14.

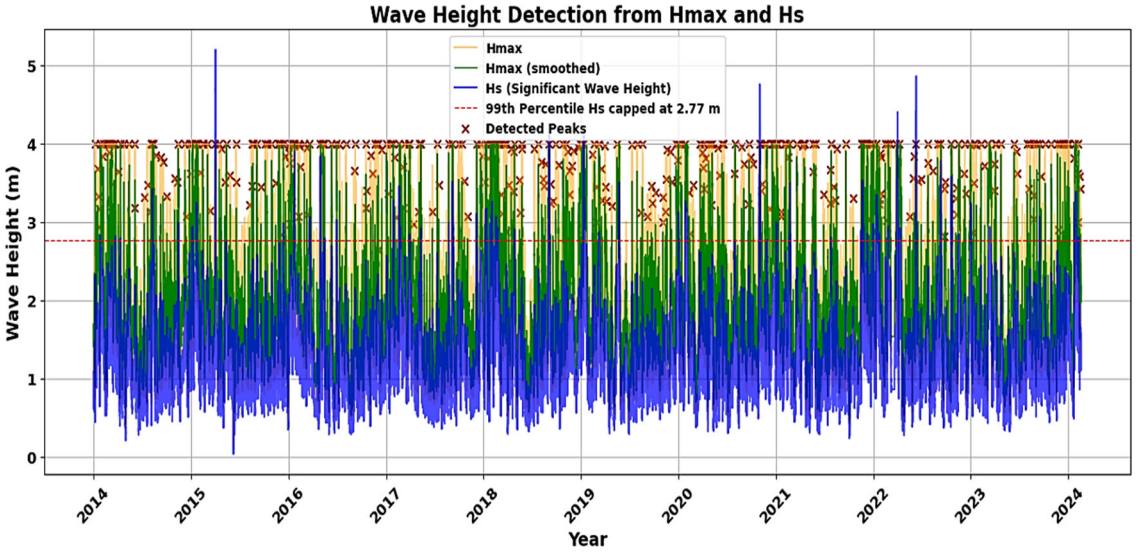

Figure 14. Tidal occurrences affecting the Maroochydore coastline using the computed threshold. The detected peaks are shown above the threshold line.

3.5. Tidal Wave Prediction Using Deep Learning

The recorded events along with the timeline were for tidal prediction using BiLSTM and CNNBiLSTM classification models. The timeseries data included zero up crossing wave period (s), peak energy wave period (s), sea surface temperature (°C), significant wave height (Hs) and maximum wave height (Hmax) as predictors for an as-detected tidal wave as the target. Table 9 shows the results of the classification prediction of tidal waves. CNNBiLSTM significantly outperforms BiLSTM across all evaluated metrics. CNNBiLSTM achieves an accuracy of 96.72%, which is higher than the 86.06% accuracy of BiLSTM. In terms of precision, CNNBiLSTM attains 93.22%, surpassing BiLSTM's 91.66%. Similarly, the recall rate for CNNBiLSTM is 94.66% which exceeds BiLSTM's 91.42%. The F1 score, which balances precision and recall, is also higher for CNNBiLSTM at 93.94%, compared to 91.54% for BiLSTM. These results indicate that integrating CNN with BiLSTM enhances the model's overall classification performance. Figure 15 shows the confusion matrix of true and predicted classes. The false positives may arise during periods of anomalous wind or pressure conditions that may mimic tidal wave precursors. This can occur during off-season weather disturbances. These patterns may not be actual tidal waves but may trigger due to their similarity to genuine events. The false negatives could occur when tidal waves begin with delayed onset signals, hence making early detection difficult. Other causes include the missing data interpolation where critical features can be obscured.

Table 9. Results of tidal wave prediction along the Maroochydore coastline using BiLSTM and CNNBiLSTM.

Metric	BiLSTM	CNNBiLSTM
Accuracy	86.06%	96.72%
Precision	91.66%	93.22%
Recall	91.42%	94.66%
F1 Score	91.54%	93.94%

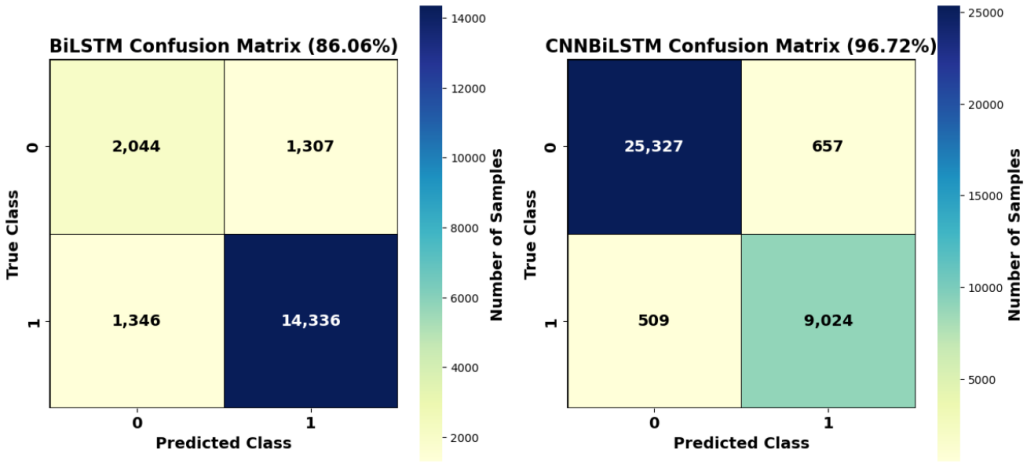

Figure 15. Confusion matrix of true and predicted classes. Darker colours show greater sample numbers.

3.6. Annual Mean of Maximum Wave Height (Hmax) Trend

The annual mean of Hmax shows an increase with a linear trend estimation, as shown in Figure 16 below. The increase of 16 mm in the maximum wave height is an important change with respect to wetland vegetation. Over time, the waves can lead to sediment redistribution, salinity variation and physical stress on the wetland plants [18,87]. Such changes in wetland conditions can also impact the resilience of these plants, leading to habitat loss. With its inability to move inward, the change in conditions will cause the loss of some wetland species [88,89]. The Maroochy River estuary is also used by migratory shorebirds, and, according to a study by Lloyd et al. [19], the roosting abundance for four species has declined significantly. The proportion of coastal inundation is likely to increase with a rise in sea level, as also found in a study [15] conducted in Sydney.

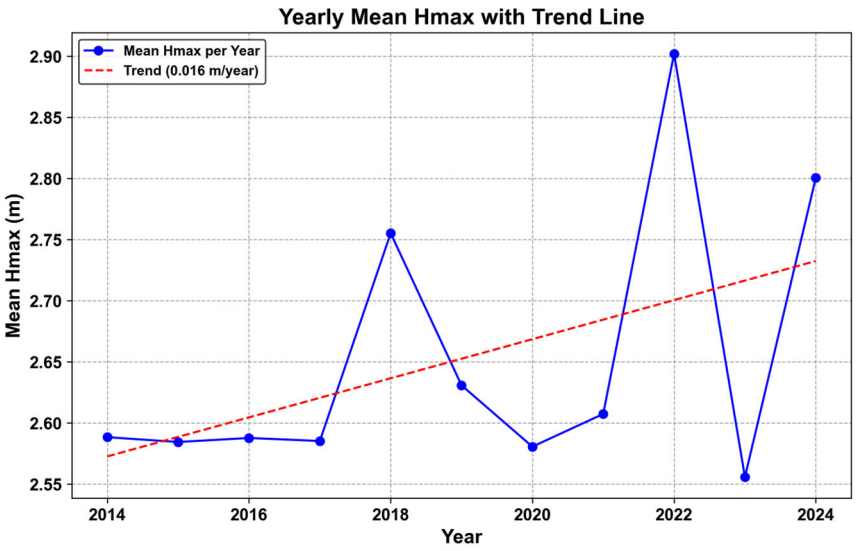

Figure 16. Annual mean of Hmax linear trend estimation from 2014 to 2024.

The spatial correlation analysis was conducted to investigate the relationship between NDVI loss zones and sea-level extremes in the Maroochydore region. The NDVI loss was calculated by comparing vegetation changes between 2015 and 2023, where a significant decrease in NDVI (less than −0.1) indicates areas of vegetation degradation, potentially due to environmental stressors such as impacts of sea-level extremes. The sea-level extremes were identified using the Global Surface Water dataset from the JRC, where areas experiencing frequent and prolonged flooding (greater than or equal to 10 months per year) were

classified as sea-level extreme zones. The JRC Global Surface Water dataset (JRC/GSW1_4) is provided by the Joint Research Centre (JRC) of the European Commission. This dataset offers insights into the spatial and temporal changes in global surface water, including the extent and occurrence of water bodies, water changes, and their variations over time. The analysis overlays these two datasets to examine the overlap between NDVI loss and sea-level extreme zones, highlighting regions where both phenomena occur simultaneously. The mean NDVI change inside and outside sea-level extremes was calculated to compare how vegetation change is influenced by the extent of sea-level flooding. The NDVI decline inside and outside the wetland is found to be 0.002 and 0.012, respectively. This means that vegetation greenness or density is decreasing both inside and outside the wetland area, but the decline is more outside the wetland area. A small negative change of 0.002, which agrees with the mean NDVI found before, could be a long-term concern, especially with the increase in extreme tidal events. It also correlates with the annual mean Hmax trend, which shows an increase in the maximum wave height in the same study region (Figure 16).

3.7. SHAP Model Evaluation and Limitations

The SHAP [90] summary plot provides an indication of each feature's importance and directional impact on the CNNBiLSTM model's predictions. Features such as Tp (peak period), Tz (zero-crossing period), and SST (sea surface temperature) show a wide spread of SHAP values, indicating that they play a significant role in influencing the model's output. The presence of both positive and negative SHAP values for these features suggests that their effect on the prediction may be varied. The high values may increase the prediction in some cases while decreasing it in others. This behaviour is crucial for understanding the model's decision-making process, especially in complex temporal–spatial data like oceanographic parameter forecasting. Moreover, the lags as input features (L1 to L5) and Hs (significant wave height) also contribute effectively to the forecasting. The colour gradient helps identify how feature values correlate with prediction impact. The red dots indicate high feature values on the positive side of the SHAP axis, indicating a strong positive contribution. The blue dots (low values) on the negative side suggest a suppressive effect. Figure 17 shows the analysis summary.

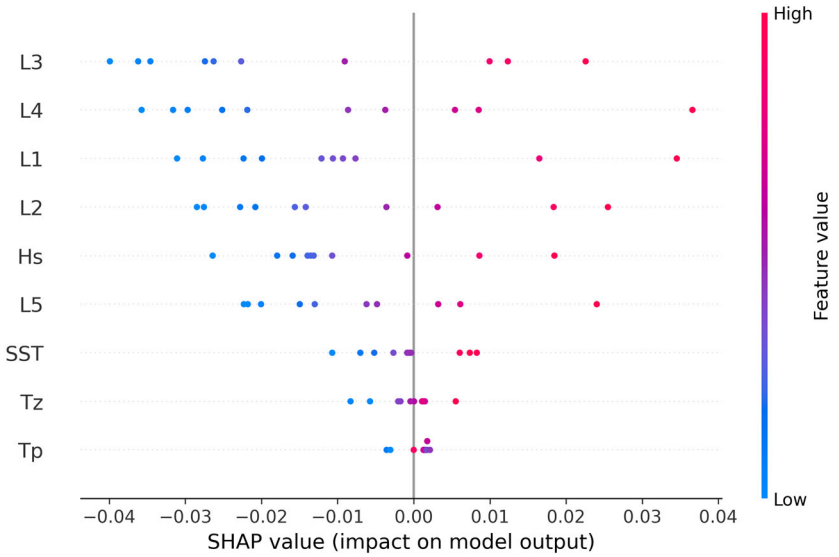

Figure 17. SHAP evaluation of CNNBiLSTM model.

Hmax forecasting, wetland change detection, and NDVI trend analysis each have inherent limitations that can affect their reliability and interpretation [91]. In Hmax forecasting, model performance is highly dependent on the quality and completeness of input

oceanic data. When using sea-level or wave datasets, missing values, sensor downtime, and gaps in historical records can affect forecast accuracy, particularly for extreme or short-lived events [91]. Wetland change detection using remote sensing can be hindered by cloud cover, seasonal variability, tidal influences, and spectral confusion with other land cover types, while mixed pixels in medium-resolution imagery reduce classification accuracy without extensive ground validation [92,93]. Similarly, NDVI trend analysis faces challenges such as saturation in dense vegetation, soil background interference in sparse areas, and atmospheric or sensor-related inconsistencies that can mimic or mask real trends [94]. In addition, missing or inconsistent timeseries data due to sensor errors or acquisition gaps can distort both seasonal and long-term vegetation assessments. Together, these limitations highlight the need for careful preprocessing, gap-filling techniques, validation, and integration of complementary datasets to improve robustness and accuracy in forecasting and wetland change detection.

4. Conclusions

This study developed an efficient hybrid deep learning model combining a Convolutional Neural Network and Bidirectional Long Short-Term Memory (CNNBiLSTM) model for the prediction of maximum sea levels. It outperformed (r = 0.9748) all three benchmark models of MLR, SVR and CatBoost with Hmax prediction in Maroochydore. To enhance thus study's maximum sea level and provide more accurate information regarding the increasing frequency and intensity of sea-level rise, this study also developed a novel CNNBiLSTM classification model to predict the occurrence of extreme tidal events with high accuracy (96.72%). The annual mean Hmax linear trend indicates a positive increase of 0.016 m/year. This was also correlated with wetland change detection using satellite Landsat data along the Maroochy River Floodplain that showed a decline of 395.64 ha from 2009 to 2023. As a potential refuge for the support of regional biodiversity due to the ongoing impact of climate change, declines of this magnitude are significant for the Maroochy River region. Programs that aim to sustain and enhance the health of vulnerable estuarine systems, encourage species diversity and limit the impact of urbanization remain important if such decal trends are likely to continue.

The findings clearly demonstrate the potential of deep learning and remote sensing integration for enhancing assessment and prediction of changes to coastal habitats with maximum sea level, tidal wave height and wetland vegetation change. This has the potential to strengthen and help better inform climate risk assessments and adaptation strategies for a diverse range of stakeholders. This study provides important contextual information for the refinement of programs aiming to support conservation and biodiversity programs. Future research could effectively extend this approach and framework to other coastal regions, incorporate real-time sensor data, or explore more advanced hybrid architectures for further performance improvements.

Author Contributions: Conceptualization, N.R.; methodology, N.R.; software, N.R.; validation, N.R.; formal analysis, N.R.; investigation, N.R.; resources, N.R.; data curation, N.R.; writing—original draft preparation, N.R.; writing—review and editing, N.R., N.S., N.D., L.S.-P.; visualization, N.R.; supervision, N.R.; project administration, N.R.; funding acquisition, N/A. All authors have read and agreed to the published version of the manuscript.

Funding: This research received no external funding.

Data Availability Statement: Data source links are shared. Datasets can be provided upon request via the authors.

Acknowledgments: The study acknowledges the publicly available datasets from Queensland Government Open Portal Oceanic Dataset, European Space Agency (ESA) WorldCover, United

States Geological Survey (USGS) EarthExplorer repository. and JRC (Joint Research Centre) of the European Commission.

Conflicts of Interest: The authors declare no conflicts of interest.

References

1. Dunn, B.; Ai, E.; Alger, M.J.; Fanson, B.; Fickas, K.C.; Krause, C.E.; Lymburner, L.; Nanson, R.; Papas, P.; Ronan, M. Wetlands insight tool: Characterising the surface water and vegetation cover dynamics of individual wetlands using multidecadal Landsat satellite data. *Wetlands* **2023**, *43*, 37. [CrossRef]
2. Ramsar Convention on Wetlands. *Scaling Up Wetland Conservation, Wise Use and Restoration to Achieve the Sustainable Development Goals*; Ramsar Convention Secretariat: Gland, Switzerland, 2018.
3. Song, X.; Zhu, Y.; Chen, W. Dynamics of the soil respiration response to soil reclamation in a coastal wetland. *Sci. Rep.* **2021**, *11*, 2911. [CrossRef] [PubMed]
4. Chen, Y.; Sun, L.; Xu, J.; Liang, B.; Wang, J.; Xiong, N. Wetland vegetation changes in response to climate change and human activities on the Tibetan Plateau during 2000–2015. *Front. Ecol. Evol.* **2023**, *11*, 1113802. [CrossRef]
5. Salimi, S.; Almuktar, S.A.; Scholz, M. Impact of climate change on wetland ecosystems: A critical review of experimental wetlands. *J. Environ. Manag.* **2021**, *286*, 112160. [CrossRef]
6. Saintilan, N.; Rogers, K.; Kelleway, J.; Ens, E.; Sloane, D. Climate change impacts on the coastal wetlands of Australia. *Wetlands* **2019**, *39*, 1145–1154. [CrossRef]
7. Mogensen, L.A.; Rogers, K. Validation and comparison of a model of the effect of sea-level rise on coastal wetlands. *Sci. Rep.* **2018**, *8*, 1369. [CrossRef]
8. Wen, L.; Hughes, M.G. Coastal wetland responses to sea level rise: The losers and winners based on hydro-geomorphological settings. *Remote Sens.* **2022**, *14*, 1888. [CrossRef]
9. Wen, L.; Glasby, T.M.; Hughes, M.G. The race for space: Modelling the landward migration of coastal wetlands under sea level rise at regional scale. *Sci. Total Environ.* **2023**, *859*, 160483. [CrossRef]
10. Rosenberry, D.O.; Hayashi, M. Assessing and measuring wetland hydrology. In *Wetland Techniques: Volume 1: Foundations*; Springer: Dordrecht, The Netherlands, 2013; pp. 87–225.
11. Guo, M.; Li, J.; Sheng, C.; Xu, J.; Wu, L. A review of wetland remote sensing. *Sensors* **2017**, *17*, 777. [CrossRef]
12. Osland, M.J.; Enwright, N.M.; Day, R.H.; Gabler, C.A.; Stagg, C.L.; Grace, J.B. Beyond just sea-level rise: Considering macroclimatic drivers within coastal wetland vulnerability assessments to climate change. *Glob. Change Biol.* **2016**, *22*, 1–11. [CrossRef] [PubMed]
13. Karmakar, S.; Islam, S.S.; Sen, K.; Ghosh, S.; Midya, S. Climate crisis and wetland ecosystem sustainability. In *Climate Crisis: Adaptive Approaches and Sustainability*; Springer: Cham, Switzerland, 2024; pp. 529–549.
14. Schuerch, M.; Kiesel, J.; Boutron, O.; Guelmami, A.; Wolff, C.; Cramer, W.; Caiola, N.; Ibáñez, C.; Vafeidis, A.T. Large-scale loss of Mediterranean coastal marshes under rising sea levels by 2100. *Commun. Earth Environ.* **2025**, *6*, 128. [CrossRef]
15. Hague, B.S.; McGregor, S.; Murphy, B.F.; Reef, R.; Jones, D.A. Sea level rise driving increasingly predictable coastal inundation in Sydney, Australia. *Earth's Future* **2020**, *8*, e2020EF001607. [CrossRef]
16. Proudfoot, M.; Singh Peterson, L. Positive SOI, negative PDO and spring tides as simple indicators of the potential for extreme coastal erosion in northern NSW. *Australas. J. Environ. Manag.* **2011**, *18*, 170–181. [CrossRef]
17. Cunningham, S.; McCutcheon, M.; Hearn, G.; Ryan, M.D.; Collis, C. *Australian Cultural and Creative Activity: A Population and Hotspot Analysis: Sunshine Coast*; Digital Media Research Centre: Brisbane, Australia, 2019.
18. Brown, M.I.; Pearce, T.; Leon, J.; Sidle, R.; Wilson, R. Using remote sensing and traditional ecological knowledge (TEK) to understand mangrove change on the Maroochy River, Queensland, Australia. *Appl. Geogr.* **2018**, *94*, 71–83. [CrossRef]
19. Lloyd, P.; Driscoll, P.V.; Bosshard, S. *Changes in Shorebird Use of the Maroochy River Estuary, Sunshine Coast, Queensland over 25 Years*; Corella: Bremen, Germany, 2024.
20. Iram, N.; Maher, D.T.; Lovelock, C.E.; Baker, T.; Cadier, C.; Adame, M.F. Climate change mitigation and improvement of water quality from the restoration of a subtropical coastal wetland. *Ecol. Appl.* **2022**, *32*, e2620. [CrossRef]
21. Powell, M.; Accad, A.; Shapcott, A. Geographic information system (GIS) predictions of past, present habitat distribution and areas for re-introduction of the endangered subtropical rainforest shrub Triunia robusta (Proteaceae) from south-east Queensland Australia. *Biol. Conserv.* **2005**, *123*, 165–175. [CrossRef]
22. Mohan, S.; Kumar, B.; Nejadhashemi, A.P. Integration of machine learning and remote sensing for water quality monitoring and prediction: A review. *Sustainability* **2025**, *17*, 998. [CrossRef]
23. Meng, H.; Zhang, J.; Zheng, Z.; Song, Y.; Lai, Y. Classification of inland lake water quality levels based on Sentinel-2 images using convolutional neural networks and spatiotemporal variation and driving factors of algal bloom. *Ecol. Inform.* **2024**, *80*, 102549. [CrossRef]

24. Zaka, M.M.; Samat, A. Advances in remote sensing and machine learning methods for invasive plants study: A comprehensive review. *Remote Sens.* **2024**, *16*, 3781. [CrossRef]
25. Morgan, G.R. sUAS and Deep Learning for High-Resolution Monitoring of Tidal Marshes in Coastal South Carolina. Ph.D. Thesis, University of South Carolina, Columbia, SC, USA, 2022.
26. Maurya, K.; Mahajan, S.; Chaube, N. Remote sensing techniques: Mapping and monitoring of mangrove ecosystem—A review. *Complex Intell. Syst.* **2021**, *7*, 2797–2818. [CrossRef]
27. Darwish, K.S. Monitoring Coastline Dynamics Using Satellite Remote Sensing and Geographic Information Systems: A Review of Global Trends. *Catrina Int. J. Environ. Sci.* **2024**, *31*, 1–23. [CrossRef]
28. Huang, W.; Dong, S. Joint distribution of significant wave height and zero-up-crossing wave period using mixture copula method. *Ocean Eng.* **2021**, *219*, 108305. [CrossRef]
29. Ahn, S. Modeling mean relation between peak period and energy period of ocean surface wave systems. *Ocean Eng.* **2021**, *228*, 108937. [CrossRef]
30. Minnett, P.J. Sea surface temperature. In *Encyclopedia of Remote Sensing*; Springer: New York, NY, USA, 2014; pp. 754–759.
31. Kumar, P.S.; Kumaraswamidhas, L.A.; Laha, S.K. Selecting effective intrinsic mode functions of empirical mode decomposition and variational mode decomposition using dynamic time warping algorithm for rolling element bearing fault diagnosis. *Trans. Inst. Meas. Control* **2019**, *41*, 1923–1932. [CrossRef]
32. García, S.; Ramírez-Gallego, S.; Luengo, J.; Benítez, J.M.; Herrera, F. Big data preprocessing: Methods and prospects. *Big Data Anal.* **2016**, *1*, 9. [CrossRef]
33. Wang, Z.; Su, X.; Wang, L.; Lang, Q.; Lu, Y.; Wang, L. A physics-guided neural network model to estimate all-sky diffuse solar radiation using Himawari-8 data. *IEEE Trans. Geosci. Remote Sens.* **2025**, *63*, 4103318. [CrossRef]
34. Chi, Y.N. Time series modeling and forecasting of monthly mean sea level (1978–2020): SARIMA and multilayer perceptron neural network. *Int. J. Data Sci.* **2022**, *3*, 45–61. [CrossRef]
35. Chi, Y.N. Time Series Modeling of Global Average Absolute Sea Level Change. *Am. J. Environ. Clim.* **2023**, *2*, 81–90. [CrossRef]
36. Wang, G. The 95 per cent confidence interval for the mean sea-level change rate derived from tide gauge data. *Geophys. J. Int.* **2023**, *235*, 1420–1433. [CrossRef]
37. Rollins Sr, D.K.; Roggendorf, A.; Khor, Y.; Mei, Y.; Lee, P.; Loveland, S. Dynamic modeling with correlated inputs: Theory, method, and experimental demonstration. *Ind. Eng. Chem. Res.* **2015**, *54*, 2136–2144. [CrossRef]
38. Raj, N.; Murali, J.; Singh-Peterson, L.; Downs, N. Prediction of Sea Level Using Double Data Decomposition and Hybrid Deep Learning Model for Northern Territory, Australia. *Mathematics* **2024**, *12*, 2376. [CrossRef]
39. Sun, Q.; Wan, J.; Liu, S.; Jiang, J.; Muhammad, Y. A new decomposition model of sea level variability for the sea level anomaly time series prediction. *J. Oceanol. Limnol.* **2023**, *41*, 1629–1642. [CrossRef]
40. Raj, N. Prediction of sea level with vertical land movement correction using deep learning. *Mathematics* **2022**, *10*, 4533. [CrossRef]
41. Song, C.; Chen, X.; Ding, X.; Zhang, L. Sea level simulation with signal decomposition and machine learning. *Ocean Eng.* **2021**, *241*, 110109. [CrossRef]
42. Nazari, M.; Sakhaei, S.M. Successive variational mode decomposition. *Signal Process.* **2020**, *174*, 107610. [CrossRef]
43. Chen, Q.; Chen, J.; Lang, X.; Xie, L.; ur Rehman, N.; Su, H. Self-tuning variational mode decomposition. *J. Frankl. Inst.* **2021**, *358*, 7825–7862. [CrossRef]
44. Alasadi, S.A.; Bhaya, W.S. Review of data preprocessing techniques in data mining. *J. Eng. Appl. Sci.* **2017**, *12*, 4102–4107.
45. Bengio, Y. Practical recommendations for gradient-based training of deep architectures. In *Neural Networks: Tricks of the Trade*, 2nd ed.; Springer: Berlin/Heidelberg, Germany, 2012; pp. 437–478.
46. Montesinos López, O.A.; Montesinos López, A.; Crossa, J. Overfitting, model tuning, and evaluation of prediction performance. In *Multivariate Statistical Machine Learning Methods for Genomic Prediction*; Springer: Cham, Switzerland, 2022; pp. 109–139.
47. Raj, N.; Prakash, R. Assessment and prediction of significant wave height using hybrid CNN-BiLSTM deep learning model for sustainable wave energy in Australia. *Sustain. Horiz.* **2024**, *11*, 100098. [CrossRef]
48. Raj, N.; Brown, J. An EEMD-BiLSTM algorithm integrated with Boruta random forest optimiser for significant wave height forecasting along coastal areas of Queensland, Australia. *Remote Sens.* **2021**, *13*, 1456. [CrossRef]
49. Trong, N.; Thanh, P.; Tinh, L.; Thao, N.; Elshewy, M. Application of Deep Learning Models for Groundwater Data Analysis: A Comparative Study of CNN (Conv1D), SimpleRNN, and Gated Recurrent Unit (GRU) Models. *Int. J. Geoinform.* **2025**, *21*, 100–114.
50. Ige, A.O.; Sibiya, M. State-of-the-art in 1d convolutional neural networks: A survey. *IEEE Access* **2024**, *12*, 144082–144105. [CrossRef]
51. Huang, R.; Wei, C.; Wang, B.; Yang, J.; Xu, X.; Wu, S.; Huang, S. Well performance prediction based on Long Short-Term Memory (LSTM) neural network. *J. Pet. Sci. Eng.* **2022**, *208*, 109686. [CrossRef]
52. Zhou, N.; Yao, N.; Li, Q. Neural Network Based on Inter-layer Perturbation Strategy for Text Classification. *Mach. Intell. Res.* **2025**, *22*, 176–188. [CrossRef]

53. Yu, Y.; Si, X.; Hu, C.; Zhang, J. A review of recurrent neural networks: LSTM cells and network architectures. *Neural Comput.* **2019**, *31*, 1235–1270. [CrossRef]
54. Reyad, M.; Sarhan, A.M.; Arafa, M. A modified Adam algorithm for deep neural network optimization. *Neural Comput. Appl.* **2023**, *35*, 17095–17112. [CrossRef]
55. Tan, H.H.; Lim, K.H. Vanishing gradient mitigation with deep learning neural network optimization. In Proceedings of the 2019 7th International Conference on Smart Computing & Communications (ICSCC), Sarawak, Malaysia, 28–30 June 2019.
56. Anam, M.K.; Defit, S.; Haviluddin, H.; Efrizoni, L.; Firdaus, M.B. Early Stopping on CNN-LSTM Development to Improve Classification Performance. *J. Appl. Data Sci.* **2024**, *5*, 1175–1188. [CrossRef]
57. Li, B.; Wang, M.; Yang, Y. Multiple linear regression with correlated explanatory variables and responses. *Surv. Rev.* **2017**, *49*, 1–8. [CrossRef]
58. Raj, N.; Gharineiat, Z. Evaluation of multivariate adaptive regression splines and artificial neural network for prediction of mean sea level trend around northern australian coastlines. *Mathematics* **2021**, *9*, 2696. [CrossRef]
59. Basak, D.; Pal, S.; Patranabis, D.C. Support vector regression. *Neural Inf. Process.-Lett. Rev.* **2007**, *11*, 203–224.
60. Smola, A.J.; Schölkopf, B. A tutorial on support vector regression. *Stat. Comput.* **2004**, *14*, 199–222. [CrossRef]
61. Awad, M.; Khanna, R.; Awad, M.; Khanna, R. Support vector regression. In *Efficient Learning Machines: Theories, Concepts, and Applications for Engineers and System Designers*; Apress: Berkeley, CA, USA, 2015; pp. 67–80.
62. Vapnik, V.; Golowich, S.E.; Smola, A.J. Support vector method for function approximation, regression estimation and signal processing. In *Advances in Neural Information Processing Systems*; MIT Press: Cambridge, UK, 1997; pp. 281–287.
63. Liu, Y.; Wang, R. Study on network traffic forecast model of SVR optimized by GAFSA. *Chaos Solit. Fractals* **2016**, *89*, 153–159. [CrossRef]
64. Preethi, D.; Khare, N. Sparse auto encoder driven support vector regression based deep learning model for predicting network intrusions. *Peer Peer Netw. Appl.* **2021**, *14*, 2419–2429. [CrossRef]
65. Hancock, J.T.; Khoshgoftaar, T.M. CatBoost for big data: An interdisciplinary review. *J. Big Data* **2020**, *7*, 94. [CrossRef]
66. Prokhorenkova, L.; Gusev, G.; Vorobev, A.; Dorogush, A.V.; Gulin, A. CatBoost: Unbiased boosting with categorical features. In *Advances in Neural Information Processing Systems*; Curran Associates Inc.: Red Hook, NY, USA, 2018; Volume 32, pp. 6639–6649.
67. Tang, F.; Mao, B.; Kato, N.; Gui, G. Comprehensive survey on machine learning in vehicular network: Technology, applications and challenges. *IEEE Commun. Surv. Tutor.* **2021**, *23*, 2027–2057. [CrossRef]
68. Joshi, A.; Saggar, P.; Jain, R.; Sharma, M.; Gupta, D.; Khanna, A. CatBoost—An ensemble machine learning model for prediction and classification of student academic performance. *Adv. Data Sci. Adapt. Anal.* **2021**, *13*, 2141002. [CrossRef]
69. Schober, P.; Boer, C.; Schwarte, L.A. Correlation coefficients: Appropriate use and interpretation. *Anesth. Analg.* **2018**, *126*, 1763–1768. [CrossRef]
70. Park, K.; Rothfeder, R.; Petheram, S.; Buaku, F.; Ewing, R.; Greene, W.H. Linear regression. In *Basic Quantitative Research Methods for Urban Planners*; Routledge: New York, NY, USA, 2020; pp. 220–269.
71. Pontius, R.G., Jr. Indices of Agreement. In *Metrics That Make a Difference: How to Analyze Change and Error*; Springer: Cham, Switzerland, 2022; pp. 85–97.
72. Zeybek, M. Nash-sutcliffe efficiency approach for quality improvement. *J. Appl. Math. Comput.* **2018**, *2*, 496–503. [CrossRef]
73. De Myttenaere, A.; Golden, B.; Le Grand, B.; Rossi, F. Mean absolute percentage error for regression models. *Neurocomputing* **2016**, *192*, 38–48. [CrossRef]
74. Hodson, T.O.; Over, T.M.; Foks, S.S. Mean squared error, deconstructed. *J. Adv. Model. Earth Syst.* **2021**, *13*, e2021MS002681. [CrossRef]
75. Shekhar, S.; Schrater, P.R.; Vatsavai, R.R.; Wu, W.; Chawla, S. Spatial contextual classification and prediction models for mining geospatial data. *IEEE Trans. Multimed.* **2002**, *4*, 174–188. [CrossRef]
76. Weigend, A.S. Time series analysis and prediction. In *Mathematical Perspectives on Neural Networks*; Psychology Press: Abingdon-on-Thames, UK, 2013; pp. 395–449.
77. Wilkinson, L. Visualizing big data outliers through distributed aggregation. *IEEE Trans. Vis. Comput. Graph.* **2017**, *24*, 256–266. [CrossRef] [PubMed]
78. Pettorelli, N. *The Normalized Difference Vegetation Index*; Oxford University Press: Oxford, UK, 2013.
79. Guo, Q.; Pu, R.; Li, J.; Cheng, J. A weighted normalized difference water index for water extraction using Landsat imagery. *Int. J. Remote Sens.* **2017**, *38*, 5430–5445. [CrossRef]
80. Taloor, A.K.; Manhas, D.S.; Kothyari, G.C. Retrieval of land surface temperature, normalized difference moisture index, normalized difference water index of the Ravi basin using Landsat data. *Appl. Comput. Geosci.* **2021**, *9*, 100051. [CrossRef]
81. Zhen, Z.; Chen, S.; Yin, T.; Chavanon, E.; Lauret, N.; Guilleux, J.; Henke, M.; Qin, W.; Cao, L.; Li, J. Using the negative soil adjustment factor of soil adjusted vegetation index (SAVI) to resist saturation effects and estimate leaf area index (LAI) in dense vegetation areas. *Sensors* **2021**, *21*, 2115. [CrossRef]

82. Vijith, H.; Dodge-Wan, D. Applicability of MODIS land cover and Enhanced Vegetation Index (EVI) for the assessment of spatial and temporal changes in strength of vegetation in tropical rainforest region of Borneo. *Remote Sens. Appl. Soc. Environ.* **2020**, *18*, 100311. [CrossRef]
83. Healthy Land & Water Ltd. Healthy Land & Water Report Card 2021. 2023. Available online: https://reportcard.hlw.org.au (accessed on 15 February 2025).
84. Cooray, P.L.; Chalmers, G.R.; Chittleborough, D. Mangrove Rehabilitation to Improve Coastal Resilience: Lessons from the Blue Heart Wetlands, Sunshine Coast, Queensland, Australia. In Proceedings of the 2nd International Conference on Mangroves for Sustainability, Kalutara, Sri Lanka, 22–23 July 2024; Centre for Environmental Studies & Sustainable Development, Open University: Colombo, Sri Lanka, 2024.
85. Huang, S.; Tang, L.; Hupy, J.P.; Wang, Y.; Shao, G. A commentary review on the use of normalized difference vegetation index (NDVI) in the era of popular remote sensing. *J. For. Res.* **2021**, *32*, 1–6. [CrossRef]
86. Jena, J.; Misra, S.R.; Tripathi, K.P. Normalized difference vegetation index (NDVI) and its role in agriculture. *Agric. Food E-Newsl.* **2019**, *1*, 387–389.
87. Lovelock, C.E.; Accad, A.; Dowling, R.M.; Duke, N.; Lee, S.; Ronan, M. *Mangroves and Saltmarshes of Moreton Bay*; The Moreton Bay Foundation: Brisbane, Australia, 2019.
88. Ballut-Dajud, G.A.; Sandoval Herazo, L.C.; Fernández-Lambert, G.; Marín-Muñiz, J.L.; López Méndez, M.C.; Betanzo-Torres, E.A. Factors affecting wetland loss: A review. *Land* **2022**, *11*, 434. [CrossRef]
89. Ross, P.M.; Adam, P. Climate change and intertidal wetlands. *Biology* **2013**, *2*, 445–480. [CrossRef] [PubMed]
90. Ponce-Bobadilla, A.V.; Schmitt, V.; Maier, C.S.; Mensing, S.; Stodtmann, S. Practical guide to SHAP analysis: Explaining supervised machine learning model predictions in drug development. *Clin. Transl. Sci.* **2024**, *17*, e70056. [CrossRef]
91. Garg, A. *Time Series Segmentation Techniques for Land Cover Change Detection*; University of Minnesota: Minneapolis, MN, USA, 2013.
92. Chan, K.K.Y.; Xu, B. Perspective on remote sensing change detection of Poyang Lake wetland. *Ann. GIS* **2013**, *19*, 231–243. [CrossRef]
93. Abdelmajeed, A.Y.A.; Albert-Saiz, M.; Rastogi, A.; Juszczak, R. Cloud-based remote sensing for wetland monitoring—A review. *Remote Sens.* **2023**, *15*, 1660. [CrossRef]
94. Sai, M.S.; Murthy, C.; Chandrasekar, K.; Jeyaseelan, A.; Diwakar, P.; Dadhwal, V. Agricultural drought: Assessment & monitoring. *Mausam* **2016**, *67*, 131–142.